Materials Advances

ROYAL SOCIETY OF CHEMISTRY

PAPER

View Article Online
View Journal | View Issue

Cite this: *Mater. Adv.*, 2020, **1**, 2310

Boosting visible light harvesting and charge separation in surface modified TiO_2 photonic crystal catalysts with CoO_x nanoclusters†

Alexia Toumazatou,[a] Maria Antoniadou,[b] Elias Sakellis,[b] Dimitra Tsoutsou,[b] Spyros Gardelis,[a] George Em. Romanos,[b] Nikolaos Ioannidis,[b] Nikos Boukos,[b] Athanassios Dimoulas,[b] Polycarpos Falaras[b] and Vlassis Likodimos*[a]

Photonic crystal structuring has emerged as a promising approach to improve the utilization of solar energy by metal oxide semiconductor photocatalysts based on the combination of slow-light, pore interconnectivity and high surface accessibility of macroporous periodic structures with judicious compositional modifications of the materials' properties. In this work, surface modification of photonic band gap engineered TiO_2 inverse opals fabricated by the convective evaporation-induced co-assembly technique was performed with nanoscale Co oxides using the chemisorption–calcination-cycle method in order to explore the interplay of metal oxide heterostructuring and photonic amplification for the development of visible light-activated photonic catalysts. Fine tuning of the films' photonic and electronic properties by controlling the inverse opal macropore size and Co oxides' loading and composition resulted in significant enhancement of the photocatalytic activity for organics decomposition under visible light, exceeding that of benchmark mesoporous TiO_2 films subjected to the same treatment. The underlying mechanism was related to the slow-photon-assisted light harvesting by low amounts of Co oxide nanoclusters that exert minimal effects on the inverse opal periodicity and texture, while enabling visible light electronic absorption and promoting charge separation *via* strong interfacial coupling on the nanocrystalline titania skeleton of the photonic crystals.

Received 15th July 2020,
Accepted 6th September 2020

DOI: 10.1039/d0ma00510j

rsc.li/materials-advances

Introduction

Semiconductor photocatalysis has been established as a promising "clean" technology for photochemical energy conversion applications, ranging from environmental pollution abatement to fuels' production, based on the utilization of solar energy and environmentally benign, earth-abundant materials.[1] Titanium dioxide (TiO_2) has been the most prominent among target photocatalytic materials, because of its strong oxidation/reduction capacity, and photochemical stability.[2] However, despite the marked progress in the development of nanostructured TiO_2 photocatalysts, alleviating titania's poor visible light harvesting, which originates from the wide band gap (3.0–3.2 eV) of TiO_2 polymorphs, along with the persistent electron–hole recombination and the consequent low photonic efficiency remains a key aspect for practical applications.[3] A straightforward, yet challenging approach to promote photon capture is by shaping TiO_2 materials in the form of photonic crystals (PCs), long established as prototype structures to control light–matter interactions.[4] Photonic crystal-assisted photocatalysis recently emerged as an advanced, structural modification for improving light harvesting

[a] *Section of Condensed Matter Physics, Department of Physics, National and Kapodistrian University of Athens, Panepistimiopolis, 15784, Greece. E-mail: vlikodimos@phys.uoa.gr*
[b] *Institute of Nanoscience and Nanotechnology, National Center for Scientific Research "Demokritos", 15341 Agia Paraskevi, Athens, Greece*

† Electronic supplementary information (ESI) available: Experimental details on materials characterization and photocatalytic evaluation. Cross sections for the PC films. Top view SEM images for CoO_x-PC406 and *R*% spectra. Ti, O, Co EFTEM maps for CoO_x-3rd-PC499. HR-TEM image and local EDX spectrum for CoO_x-1st-PC406. Raman spectra for CoO_x-modified P25 and PC films at 514 nm. Kubelka–Munk *F*(*R*) spectra for CoO_x-P25. Ti 2p XPS for CoO_x-PC499 and CoO_x-P25 films. MB photodegradation kinetics under UV-Vis and visible light, MB dark adsorption and kinetic constants $k_{UV\text{-}Vis}$ and k_{Vis}. Visible light SA photodegradation kinetics, apparent kinetic constants k_{Vis} and SA dark adsorption. Wavelength-dependent SA reaction rates for CoO_x-1st-PC films. Stability tests on MB photodegradation under UV-Vis light and SEM images after each cycle for CoO_x-1st-PC406. HR-TEM for CoO_x-2nd-PC406 and Co 2p XPS for CoO_x-3rd-PC406 before and after SA photodegradation. PL spectra of CoO_x-PC499. Spectral deconvolution of DMPO spin trap EPR spectra for PC suspensions in ACN and spin trap EPR spectra of DMPO/PC dispersions in water and in the presence of 10% DMSO. Elemental EDX analysis for CoO_x-modified PC and P25 films. See DOI: 10.1039/d0ma00510j

of photocatalytic nanomaterials by means of the slow photon effect, *i.e.* light propagation with reduced group velocity for wavelengths near the photonic band gap (PBG) or stop band (in the case of incomplete PBG) edges.[5] Progress in the fabrication of metal oxide PCs based on bottom-up colloidal self-assembly techniques,[6] furnished fertile ground for the development of highly efficient UV and recently visible light activated (VLA) photonic catalysts.[7–9] These materials combine the unique potential for slow-photon-assisted light harvesting, mass transport and adsorption of macroporous periodic structures, such as inverse opals,[10] with compositional tuning of the catalysts' properties for enhanced charge separation and visible light activation.[7] The fundamental amplification mechanism is based on PBG engineering that enables spectral overlap of the slow-photon regime with the photocatalyst' electronic absorbance leading to the extension of the optical path length for incident photons within the periodic network, while evading Bragg reflection losses.

Heterostructuring titania inverse opals with narrow band gap semiconductors such as metal chalcogenide[11–14] and metal oxide (MO)[15–17] nanocrystals has been a competent approach to combine visible light activation and interfacial charge transfer with slow-photon amplification in macroporous PC catalysts. Marked improvements of the photocatalytic performance due to slow-photon effects were identified in CdS-sensitized SnO_2[12] and ZrO_2[13] PCs under visible light, when the CdS electronic absorption edge overlapped with the stop band edge of the photocatalytically inert, wide band gap PC supports. Likewise, matching the stop band edge of TiO_2 PCs with the electronic absorption of infiltrated Cu_2O nanocrystals resulted in the acceleration of photocatalytic kinetics.[15] Surface modification of TiO_2 by ''molecular'' metal oxide nanoclusters has been a promising means for the development of solar environmental catalysts, offering high visible-light photocatalytic activity without compromising their performance under UV light.[18] Controlled deposition of extremely small MO clusters on titania's surface by the chemisorption–calcination-cycle (CCC) technique has been demonstrated by Tada *et al.*[19] based on the strong adsorption of metal acetylacetonate complexes on TiO_2[20] followed by meticulous removal of physisorbed molecules and post-thermal oxidation of the organic part. Thorough investigations of molecular-scale MO–TiO_2 photocatalysts have shown that broadband visible light activation could be achieved by raising titania's valence band *via* interfacial M–O–Ti bonds forming surface states, without introducing impurity states of low oxidation potential.[21] Band gap engineering by the CCC method resulted in the development of highly efficient MO–TiO_2 photocatalysts under visible and UV light with those comprising ultrafine Co_2O_3 nanoclusters presenting the highest VLA photocatalytic and thermocatalytic efficiencies among nanoparticulate systems.[22] Nanoscale cobalt oxides (CoO_x) have been also attracting much attention owing to their exceptional performance as standalone electrocatalysts[23,24] or co-catalysts[25,26] for the oxygen evolution reaction. Among them, the most prominent catalyst has been the mixed-valence Co_3O_4 spinel, whose electronic structure was only recently resolved to possess a direct band gap in the near infrared (NIR) region of *ca.* 0.8 eV.[27,28] This band is accompanied by strong ligand-to-metal and metal-to-metal charge transfer transitions in the visible range at *ca.* 2.8 and 1.7 eV lower than the band gaps (1.8 and 2.5–2.7 eV) of the single valence Co_2O_3 and CoO oxides, respectively.[29] Moreover, the presence of intrinsic point defects, especially Co vacancies acting as acceptors,[30] render Co_3O_4 a p-type semiconductor that can be combined with n-type ones for the formation of efficient p–n heterojunction photocatalysts.[31,32] However, this was not the case for Co_3O_4–TiO_2, where titania's conduction band was reported to shift below the redox potential for H_2 evolution and Co_3O_4 acts as hole scavenger.[33,34]

In this work, nanoscale CoO_x surface modification of PBG engineered TiO_2 inverse opal films, fabricated by the convective evaporation-induced co-assembly technique, was performed for the first time by the CCC method in order to exploit the interplay of photonic enhancement and visible light activation for the development of efficient VLA photonic catalysts. Fine tuning of the films' photonic and electronic properties was achieved by varying the inverse opal diameter and the number of chemisorption–calcination cycles that control the CoO_x concentration and composition. This resulted in significant improvement of the VLA photocatalytic activity for the modified CoO_x–TiO_2 PC films on the degradation of methylene blue and salicylic acid for low CoO_x loading. The observed amplification was related to the synergy of slow-photon-assisted light harvesting of the macroporous inverse opal films with the enhanced charge separation and visible light absorption of CoO_x nanoclusters.

Experimental

Materials

Monodisperse poly(methyl methacrylate)–PMMA spheres with mean diameters of 260, 406 and 499 nm were purchased from Microparticles GmbH in the form of colloidal dispersion of 5% solids (w/v) in deionized (DI) water (2.0–2.4% CV). Titanium(IV) bis(ammonium lactato)dihydroxide (TiBALDH) 50 wt% aqueous solution and the spin trap 5,5-dimethyl-1-pyrroline *N*-oxide (DMPO) were obtained from Sigma Aldrich, while cobalt(II) acetylacetonate dihydrate $Co(acac)_2(H_2O)_2$ was purchased from TCI. All other reagents were of analytical or ACS reagent grade.

TiO_2 inverse opal fabrication

Titania inverse opals were deposited by the convective evaporation-induced co-assembly of sacrificial polymer spheres with the hydrolyzed TiBALDH sol–gel precursor,[35,36] as shown in Scheme 1. Thereby, the sequential steps of template self-assembly and liquid phase infiltration conventionally used for inverse opal preparation are combined into a single-step process yielding more robust photonic films. Typically, cleaned glass slides were nearly vertically suspended in 20 ml of 0.125 wt% PMMA sphere suspension and 0.14 ml of fresh precursor (0.25 ml TiBALDH solution, 0.5 ml HCl 0.1 M and 1 ml EtOH), both sonicated for 30 min before use. They were kept at 55 °C until the solvent fully evaporated over 3 days, producing composite films that comprised the titania gel within the PMMA opal interstitial space. The dry films were calcined at

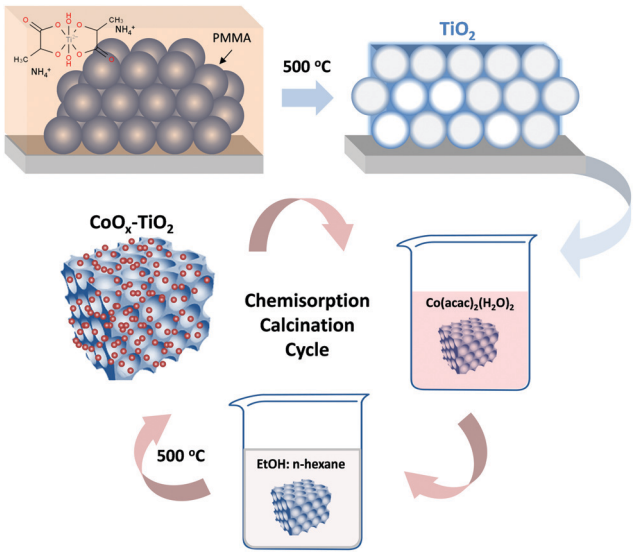

Scheme 1 Schematic illustration of the fabrication process for CoO_x–TiO_2 inverse opal films.

500 °C for 2 h in air (1 °C min^{-1}), to remove the PMMA matrix and crystallize titania in the inverse replica structure. The TiO_2 PC films were labeled as PC260, PC406 and PC499 after the diameter of the templating PMMA spheres.

Mesoporous TiO_2 reference films were deposited on glass slides by spin coating (1000 rpm, 60 s) paste of the benchmark Aeroxide® P25 nanopowder[37] in order to validate the photonic materials' performance. After drying at 120 °C (15 min), the films were annealed at 450 °C (30 min) in air. The deposition was repeated twice in order to increase the film thickness.

CoO_x surface modification

Surface modification by the CCC method (Scheme 1) was performed by immersing the titania PC and reference films to 100 ml of a 1 mM $Co(acac)_2(H_2O)_2$ solution (3 : 17 v/v EtOH : *n*-hexane) for 24 h at 25 °C.[22] The modified films were repeatedly washed with the same solvent in order to remove physisorbed Co(acac) complexes leaving the chemisorbed ones *via* ligand-exchange between the acetylacetonate H_2O group and the hydroxylated TiO_2 surface.[19] The calcination step was performed by heating (1 °C min^{-1}) the dried films in air at 500 °C for 1 h to allow for Co–O–Ti interfacial bond formation.[18] The CC modification was repeated up to three cycles and the corresponding PC films were designated as CoO_x-*n*th-PC*XXX* with *XXX* = 260, 406, 499 being the PMMA diameter and *n* the CC cycle index.

Materials characterization and photocatalytic evaluation

The morphological, structural, optical and electronic properties of the pristine and modified films were characterized by scanning electron microscopy (SEM) coupled with energy-dispersive X-ray spectroscopy (EDX), transmission electron microscopy (TEM), Raman, photoluminescence (PL) and X-ray photoelectron spectroscopies (XPS), diffuse and specular reflectance, standard BET and pore size analysis with N_2 porosimetry, photoelectrochemical and spin-trap electron paramagnetic resonance (EPR) measurements (see detailed description in S1, ESI†). The photocatalytic activity of the photonic and reference films was evaluated on the aqueous phase degradation of methylene blue (MB) (Alfa Aesar) and salicylic acid (SA) (Sigma-Aldrich) as model water pollutants under UV-Vis and visible light, as detailed in S2, ESI.†

Results and discussion

Structural and optical properties

Fig. 1 presents comparative top-view SEM images of the co-assembled TiO_2 photonic films from colloidal PMMA spheres of different diameters. The formation of long-range ordered three dimensional (3D) inverse opals was evidenced,

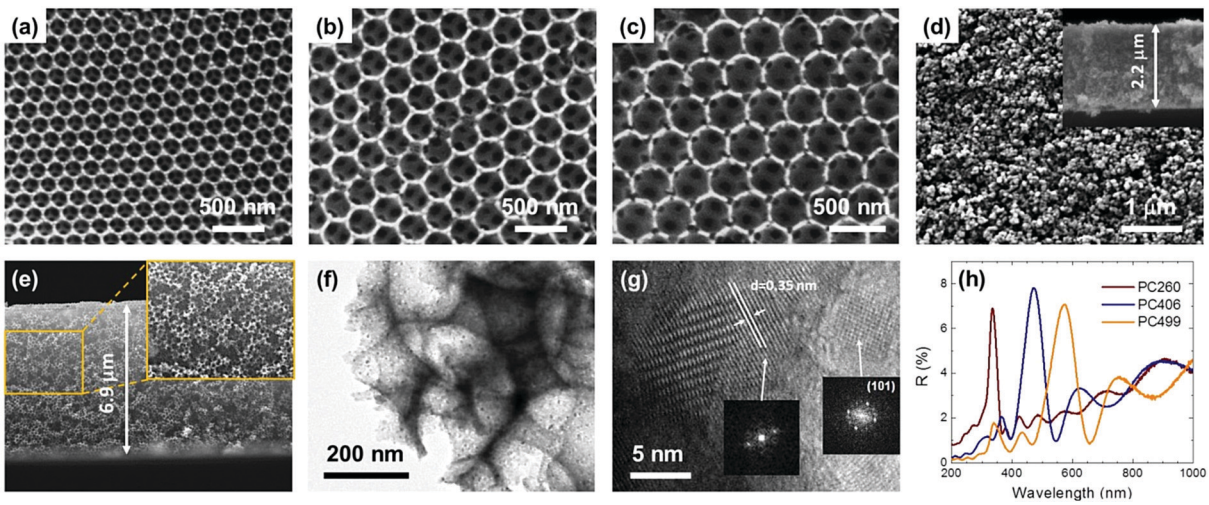

Fig. 1 Top view SEM images of the (a) PC260, (b) PC406, (c) PC499 TiO_2 inverse opals in comparison with the (d) mesoporous P25 films (the inset shows the corresponding cross section). (e) Cross section of PC260 films. (f) and (g) TEM images of the PC499 inverse opal at different magnifications. The insets in the high-resolution TEM (HR-TEM) image (g) show the fast Fourier transform (FFT) patterns of the indicated areas. (h) Specular reflectance (*R*%) spectra of the PC films at 15° incident angle.

corresponding to the (111) planes of an fcc lattice of spherical void macropores (in the place of the sacrificial polymer spheres) surrounded by a solid skeleton that fills the interstitial space. The macroporous periodic structure contrasts that of the P25 reference exhibiting a rough, sponge-like morphology, characteristic of mesoporous films (Fig. 1d). The PC macropores were interconnected through smaller ones (dark circular areas of 50–70 nm diameter) creating open windows at the contact points of adjacent spheres after calcination, which are essential for the mass transport within the pore network. The macropore size increased with the PMMA diameter, though the obtained values were considerably smaller, *ca.* 60%, than those of the polymer template, reflecting the persistent volume shrinkage due to the amorphous-to-crystalline phase transition that occurs during calcination.[38] The thickness of the PC films, which extended over several tens of microns, was *ca.* 6.5 μm (Fig. 1e and Fig. S1, ESI†), while the P25 film thickness was approximately 2.2 μm (inset of Fig. 1d), leading to comparable, though higher, by ~20%, titania mass loading to that of the macroporous PCs.

TEM images showed that the PC skeletal walls were mesoporous, consisting of aggregated anatase nanocrystallites of size ≤10 nm, identified by the characteristic (101) planes of the anatase titania phase by HR-TEM analysis (Fig. 1g). The relatively thick (*ca.* 30 nm) nanocrystalline walls with respect to the constituent anatase nanoparticles, could thus produce hierarchical pore structure architectures inducing a secondary mesoporosity to the PC skeleton that is crucial for the film's surface area and photocatalytic performance.[10]

PBG formation was evidenced by the specular reflectance (R%) spectra for the inverse opal films at 15° incident angle, as shown in Fig. 1h. A distinct reflectance peak was resolved in all R% spectra that shifted to higher wavelengths with the increase of macropore size (Table 1). This variation is characteristic of stop band formation for wave propagation along the [111] direction in TiO_2 inverse opals.[7] In addition, Fabry–Pérot interference fringes were observed at frequencies outside PBG, indicating the relative uniformity of PC domains within the probed areas (<1 mm^2). The PBG positions can be described by modified Bragg's law for first order diffraction from the (111) fcc planes,[7] from which the PC's effective refractive index n_{eff} and solid filling fraction $1 - f$ (f = 0.74 for the ideal fcc lattice) were determined in air (Table 1) using the experimental stop band wavelengths along with the measured diameters (S1, ESI†). Titania's filling fractions were appreciably smaller than the theoretical value of 0.26 for complete filling of the inverse fcc lattice, corroborating the nanocrystalline nature and mesoporosity of the anatase walls. Moreover, the $1 - f$ values decreased for larger macropores, reflecting the relative thinning of the skeletal walls with respect to the spherical voids, which affects the surface area and CoO_x growth by the CCC method (*vide infra*). Furthermore, using the obtained filling fractions and the refractive index of water (n_{H_2O} = 1.33), the stop band positions were calculated for the PC films in water (Table 1), where the photocatalytic reaction takes place.

Surface modification by consecutive CC deposition cycles of $Co(acac)_2(H_2O)_2$ had no appreciable effect on the macropore size and specular R% spectra of the photonic films (Fig. S2, ESI†). Energy filtered TEM (EFTEM) elemental analysis was applied to identify the presence of Co species and their distribution on the nanocrystalline anatase walls of the CCC modified inverse opals, as shown in Fig. 2a–c. Ti and Co elemental maps of the area corresponding to the bright field TEM image of CoO_x-2nd-PC406 verified the uniform spatial deposition of Co that presented comparable dispersion to that of Ti, while similar results were obtained for the Co distribution on CoO_x-3rd-PC499 (Fig. S3, ESI†). Furthermore, HR-TEM images of the nanocrystalline walls for the modified inverse opals revealed the presence of dark inclusions of *ca.*1 nm size among the anatase nanoparticles, as shown in Fig. 2d for PC499 3rd, which were not resolved in the HR-TEM images of the pristine PC films (Fig. 1f). These nanoscale deposits, whose crystallinity could not be discerned, indicate the formation of ultrafine CoO_x species, consistent with the "molecular" MO cluster size

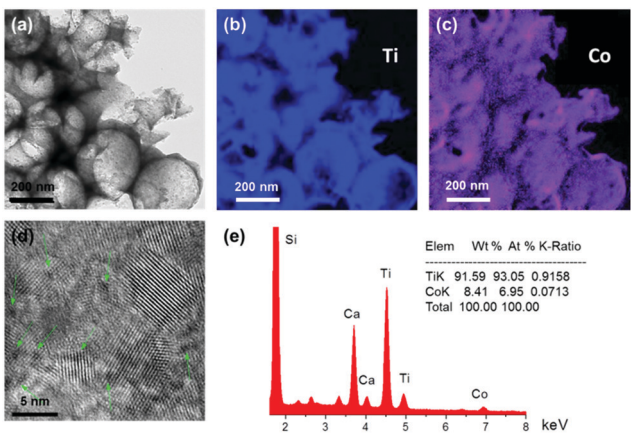

Fig. 2 (a) Bright field TEM image for CoO_x-2nd-PC406 and the corresponding (b) Ti and (c) Co EFTEM elemental maps. (d) HR-TEM image of CoO_x-3rd-PC499 with arrows depicting dark inclusions of *ca.* 1 nm size among the anatase nanoparticles. (e) The corresponding EDX spectrum and Ti K, Co K elemental analysis for CoO_x-3rd-PC499.

Table 1 Structural and optical properties of the TiO_2 photonic films

Film	D_{PMMA}[a] (nm)	D[b] (nm)	$\lambda_{exp}(15^\circ)$[c] (nm)	n_{eff} (air)	$1 - f$[d]	n_{eff} (H_2O)	$\lambda(0^\circ)$[d] (air)	$\lambda(0^\circ)$[d] (H_2O)
PC260	260	150	335	1.39	0.170	1.60	341	393
PC406	406	250	472	1.18	0.073	1.45	484	594
PC499	499	310	573	1.16	0.062	1.44	587	727

[a] D_{sphere}: diameter of the colloidal PMMA spheres. [b] D: macropore diameter of the TiO_2 PC films determined by SEM. [c] $\lambda_{exp}(15^\circ)$: PBG position determined from the 15° incidence specular spectra. [d] $\lambda(0^\circ)$: PBG position calculated from modified Bragg law at $\theta = 0^\circ$ incidence.

featured by the CCC method.[18] It should be noted that local EDX elemental analysis in the HR-TEM images of CoO_x-1st-PC406 (Fig. S4, ESI†), where the dark spots could be hardly discerned, verified the presence of Co. This suggests that both highly dispersed and aggregated CoO_x clusters, especially after the 2nd and 3rd CC cycles, are present in the CoO_x-PC films. The variation of Co species content was quantified by EDX analysis based on the Ti K and Co K peaks for the modified PC films (Fig. 2e). The obtained results showed that the Co loading amount increased almost linearly with the number of cycles (Table S1, ESI†). Among all films, PC260 with the smallest macropore size and the P25 films presented the highest Co (at%) values indicating that the films' texture is essential for CoO_x nanocluster growth on the nanocrystalline inverse opal walls.

The pore structure of the titania inverse opals was assessed by LN_2 porosimetry analysis, summarized in Fig. 3 and Table 2.

Significantly enhanced surface areas were derived by multi-point BET analysis for the pristine PCs, the highest reaching 144 $m^2\ g^{-1}$ for PC260, reflecting mostly the wall mesoporosity arising from the inter-crystallite void space between the anatase nanoparticles rather than the large macropores. The mean spherical pore size (d_{mean}) was accordingly underrated compared to the macropore size determined by SEM (Table 1), since the BET surface area comprises largely the contribution of mesopores in the internal surface of the nanocrystalline TiO_2 skeleton. Increase of the macropore size resulted in the drop of both surface area (~55%) and total macropore volume (Table 2), complying with the variation of the filling fraction, where an analogous reduction was derived for PC406 and PC499 (Table 1). The extension of accessible surface area at smaller macropores could also assist the adsorption of $Co(acac)_2(H_2O)_2$ molecules on the skeletal walls, in agreement with the Co (at %) pore size dependence for the PC films (Table S1, ESI†), where significant enhancement was observed for PC260.

In addition, CoO_x deposition resulted in diverse effects on the inverse opal pore structure, namely a drastic reduction (27%) of the high surface area for PC260 and an increase, at different extents, for PC406 (33%) and PC499 (5%).

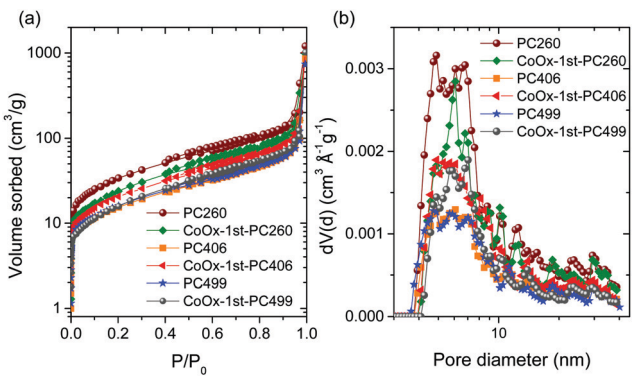

Fig. 3 (a) Adsorption–desorption N_2 isotherms at 77.4 K and (b) pore size distributions derived from the NLDFT model for the pristine and CCC modified TiO_2 inverse opals.

Table 2 Pore structure characteristics of the pristine and modified photonic films

Film	BET ($m^2\ g^{-1}$)	TPV[a] ($ml\ g^{-1}$)	d_{mean}[b] (nm)	d_{NLDFT}[c] (nm)	V_{meso} ($ml\ g^{-1}$)
PC260	143.6	1.87	78	48.87	0.299
PC406	64.1	1.33	125	60.79	0.143
PC499	68.6	1.14	100	47.28	0.138
CoO_x-1st-PC260	105.0	1.52	87	60.79	0.239
CoO_x-1st-PC406	85.0	1.58	111	48.87	0.189
CoO_x-1st-PC499	72.1	1.58	132	70.32	0.155

[a] Total pore volume determined at 0.995 relative pressure. [b] The mean pore size d_{mean} is derived as $d_{mean} = 6\cdot(TPV)/(BET)$. [c] The pore size derived from the PSDs using the NLDFT-N_2-silica adsorption branch kernel at 77 K based on a cylindrical pore model for pores of diameter <5 nm, and spherical pores of diameter >5 nm.

This could be related to the partial blocking of the abundant mesopores in the PC260 skeleton with CoO_x loading. On the other hand, the lower CoO_x uptake on PC406 and PC499 films with the larger macropores seems to promote wall mesoporosity and the resulting surface area. Furthermore, NLDFT pore size analysis for the pristine and modified PCs showed that the width of the pore size distributions (PSDs) consisting of mesopores in the range of 5–7 nm, presented weak variations with the macropore size and CoO_x loading (Fig. 3b). On the other hand, the mesopore volume (V_{meso}) decreased significantly with the macropore size reflecting the reduction of available interfaces for the larger spherical voids.[39] Moreover, CoO_x loading caused a drastic reduction of V_{meso} for CoO_x-1st-PC260 in contrast to its increase for the larger macropore PCs, most prominent for CoO_x-1st-PC406, following the corresponding BET variation.

The structural properties and phase composition of the pristine and CCC modified films were investigated by Raman spectroscopy. Fig. 4 (upper panel) compares the Raman spectra of PC260, PC406, PC449, and P25 films, before and after three successive CC cycles at 785 nm. All PC films exhibited the characteristic Raman-active phonons of anatase TiO_2 at approximately 147 (E_g), 197 (E_g), 398 (B_{1g}), 518 (A_{1g} + B_{1g}), and 642 cm^{-1} (E_g).[40] No Raman bands arising from PMMA and carbonaceous residues or other TiO_2 polymorphic phases such as rutile or brookite could be traced, indicating that all inverse opals crystallized in the single anatase phase after calcination at 500 °C. The anatase modes presented significant shifts and broadening for all PCs compared to the P25 films. The most pronounced change was detected for the low frequency E_g mode that shifted to 147 cm^{-1} with full-width at half-maximum (FWHM) of 17 cm^{-1} at 514 nm, compared to the values of 144 cm^{-1} and FWHM = 12 cm^{-1} for P25 (Fig. S5a, ESI†). These differences can be related to the breakdown of the $q = 0$ selection rule and the associated size effects in the Raman spectra of titania nanomaterials.[41] Using the corresponding E_g frequency *vs.* FWHM correlation curves,[40,41] the formation of *ca.* 8 nm anatase nanocrystallites is predicted for the PCs, considerably smaller than those (~20 nm) reported for P25. This agrees with the HR-TEM analysis and recent results on the co-assembly of TiO_2 inverse opals,[42] indicating that the confined sol–gel reaction of the water soluble TiBALDH precursor

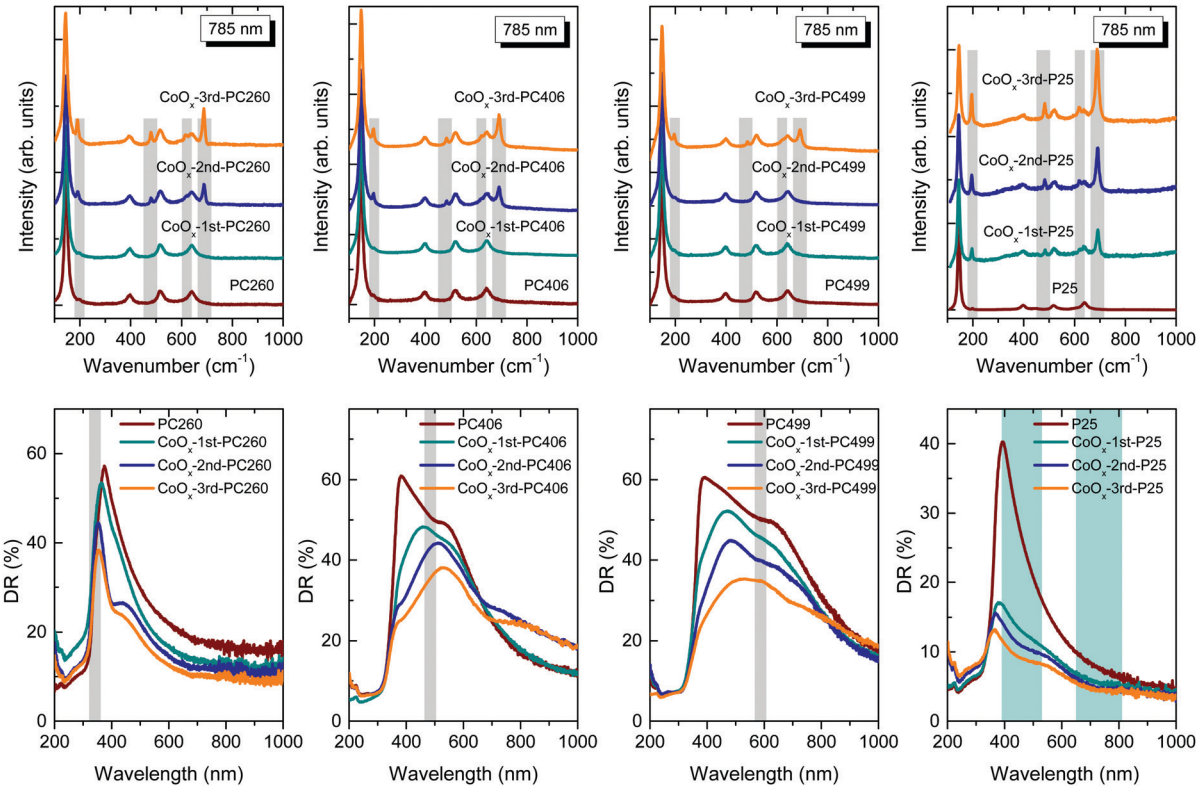

Fig. 4 (upper) Micro-Raman spectra at 785 nm and (lower) diffuse (DR%) reflectance spectra of the CoO_x-modified PC260, PC406, PC449, and P25 films. The narrow grey-shaded bands in the Raman spectra highlight the evolution of the Co_3O_4 phonon modes, while the corresponding shaded bands in the DR% spectra depict the stop band positions of the PC films according to modified Bragg law at $\theta = 0^\circ$ (Table 1) with width estimated from the FWHM of the 15° incidence *R*% peak. The cyan-shaded areas in the DR% spectra of the CoO_x-P25 films indicate the Co_3O_4 electronic absorption bands.

within the opal interstices impedes anatase growth and leads to small ($\leq$10 nm) nanocrystals, in spite of the relatively high calcination temperature of 500 °C.

Except for the anatase phonons, a series of new Raman bands emerged at 194, 483, 619 and 692 cm^{-1} upon consecutive CC cycles for all films. These bands can be identified with the characteristic F_{2g}, E_g, F_{2g} and A_{1g} Raman modes of Co_3O_4 crystallizing in the spinel structure,[43] with the missing, relatively weak, F_{2g} mode at 522 cm^{-1} being masked by the anatase 518 cm^{-1} band (Fig. S5b–d, ESI†). This assignment is supported by the strong intensity enhancement of the Co_3O_4 modes under 785 nm excitation (Fig. 4) compared to those at 514 nm (Fig. S5b–d, ESI†).

This can be explained by the close match of the near infrared laser excitation (785 nm) to the strong electronic absorption of the Co_3O_4 spinel near 750 nm and the resulting resonance Raman effect. More importantly, the relative intensity of the Co_3O_4 Raman bands with respect to the anatase ones increased with the CC cycles following a distinct dependence on the PC macropore size (Fig. 4). In particular, Co_3O_4 was identified in CoO_x-PC260 and CoO_x-PC406 after the 2nd cycle, in contrast to CoO_x-PC499, where the spinel phase appeared only after the 3rd cycle. The highest Co_3O_4 Raman intensity was observed for CoO_x-PC260 correlating with the enhancement of surface area and wall mesoporosity (Table 2) as well as its relatively higher Co (at%) content (Table S1, ESI†). On the other hand, the relative Co_3O_4 Raman intensity was reduced for the lower surface area inverse opals, especially the PC499 one. Considerably higher Raman intensities were observed for the CoO_x-P25 films, even for the 1st cycle, despite their similar Co loading to the PC260 films (Table S1, ESI†), indicating that the size and texture of the supporting titania nanoparticles is crucial for the growth of the Co_3O_4 phase. Nevertheless, the formation of single valence CoO and Co_2O_3 oxides on the anatase PC walls after the 1st cycle, where appreciable amounts of Co loading (2.4–4.5 Co at%) were detected by EDX (Table S1, ESI†), cannot be excluded since both of them are rather weak Raman scatterers. Specifically, first-order Raman scattering is formally forbidden for the rock-salt centrosymmetric CoO crystal structure allowing only weak second-order and defect-induced Raman modes,[44] whereas similar Raman spectra to Co_3O_4 have been reported for the less stable Co_2O_3 phase.[45] The nature of CoO_x species was further explored by laser annealing experiments on the PC 1st cycle films. To this aim, the 785 and 514 laser beams were focused on the films at full power (S1, ESI†) in order to induce local overheating that may drive the oxidation of CoO_x to the stable Co_3O_4 phase in the laser focal area.[44] Raman spectra successively acquired on the same spot showed no difference to the initial ones, corroborating the presence of poorly crystallized, nanoscale CoO_x species for the 1st CC cycle.

Fig. 4 (lower panel) shows the diffuse reflectance (DR%) spectra of the CoO_x-modified PC and P25 films, before and after

three CC cycles. An intense, broad DR% band was clearly resolved for PC499 and PC406 along with a weak shoulder for PC260, following the corresponding PBG variation, contrary to the constant anatase absorption edge at 375 nm and the featureless spectra of P25 films at $\lambda > 400$ nm. Both the intensity and width of the DR% peak were markedly higher than the corresponding specular ones due to the contribution of PC domains of different thickness within the area probed by the coarse focused beam (spot area of *ca.* 2 mm^2). In addition, the DR% bands were systematically red-shifted with respect to the stop bands derived from the *R*% spectra (Fig. 3), reflecting the longer optical path and the resulting diffuse scattering at the low-energy PBG edges, where "red" slow photons are expected to localize in the high refractive index part of the PC, *i.e.* the titania skeleton.[42] The DR% intensity was progressively reduced with the CC cycles for both CoO_x-PC and CoO_x-P25 films. For the latter, which presented the most pronounced DR% drop, the corresponding absorbance spectra (Fig. S6, ESI†), estimated from the Kubelka–Munk transform, revealed the gradual appearance of two broad bands at *ca.* 450 and 750 nm. These bands are in close agreement with the charge transfer transitions of Co_3O_4,[27] identified by Raman from the 1st cycle in P25 films. On the other hand, the DR% spectra of the CoO_x-PC films were relatively less affected compared to CoO_x-P25, especially for the 1st cycle, where no trace of Co_3O_4 could be resolved by Raman. In addition, the modified PC406 and PC499 inverse opals, where Co_3O_4 formation was relatively inhibited, presented the most noticeable DR% reduction in the range of 400–500 cm^{-1} after the 1st CC cycle, implying the preferential formation of the higher energy band gap CoO (~2.6 eV) and Co_2O_3 (~1.8 eV) oxides.[29]

Comparative XPS measurements were further performed on the CoO_x-modified PC499 and P25 films presenting the lowest and highest Co_3O_4 contents, respectively, in order to investigate the Co oxidation state. Fig. 5 shows the evolution of the XP Co 2p core level spectra, where appreciable signal could be detected only after the 2nd cycle, while the corresponding Ti 2p spectra confirmed the presence of stoichiometric Ti^{4+} ions for all films (Fig. S7, ESI†). In order to enhance surface sensitivity and maximize the Co 2p signal, XPS were recorded at 68° for CoO_x-3rd-PC499. In that case, the main Co $2p_{3/2}$ peak was located at 780.2 eV, which is indicative of both Co^{2+} and Co^{3+} ions, *i.e.* CoO and Co_2O_3 species, respectively.[46] Nevertheless, a satellite (S) peak could be traced in the surface sensitive 68° XP spectra at +6.48 eV from the main Co $2p_{3/2}$ peak. This value points to the formation of Co_2O_3 (6.3 eV) rather than CoO, where the S peak should have come at +7.9 eV from the main one, in agreement with the previous results on CCC modified anatase nanoparticles.[22] On the other hand, the main Co $2p_{3/2}$ peak shifted to lower binding energies at ~779.8 eV or lower for the CoO_x-P25 films, indicative of the preferential formation of the Co_3O_4 spinel, in agreement with the Raman results.

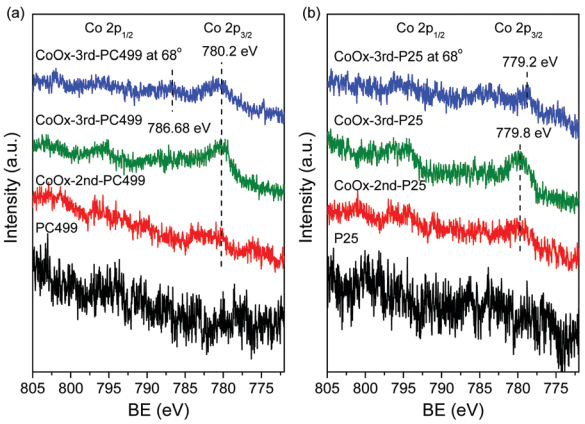

Fig. 5 Co 2p XP spectra for pristine and CoO_x-modified (a) PC499 and (b) P25 films.

Photocatalytic activity

The photocatalytic performance was initially evaluated on MB dye degradation for the CoO_x-modified PC406 and PC499 films with PBGs close to the CoO_x electronic absorption bands in the visible range (Table 1), in comparison to the corresponding mesoporous CoO_x-P25 films under UV-Vis and visible light (Fig. 6a–c). For all films, the $\ln(C/C_0)$ *vs.* *t* plots exhibited linear behaviour under both illumination conditions indicating that MB photodegradation followed pseudo first-order kinetics (Fig. 6a and b). The apparent kinetic constants $k_{UV\text{-}Vis}$ and k_{Vis} determined from the slopes of the corresponding linear plots and the original C/C_0 *vs.* *t* curves for the different titania films are presented in Fig. S8a and b, ESI.† The dye concentrations C_0 after dark adsorption of the cationic MB dye on the PC and P25 films varied considerably (Fig. S8c, ESI†) following closely the variation of the films' surface area (Table 2). In order to evade the resulting concentration dependence of the apparent kinetic constants $k_{UV\text{-}Vis}$ and k_{Vis}, the reaction rates *r* were used to quantify the films' photocatalytic activity.[47] It is worth noting that for pseudo first-order kinetics and low (<mM) MB concentrations, the reaction rate is proportional to C_0 according to $r = kC_0$. Fig. 6c displays the obtained rates, $r_{UV\text{-}Vis}$ and r_{Vis}, for the pristine and CoO_x-modified PC and P25 films under UV-Vis and visible light as a function of the CoO_x loading amount (Table S1, ESI†). Comparison between the unmodified films' performance showed significant improvement of both $r_{UV\text{-}Vis}$ and r_{Vis} for the inverse opals, most prominent for PC406 that exceeded the benchmark P25 films. This distinct enhancement has been related to the slow-photon amplification mechanism in dye sensitized photocatalysis for TiO_2,[48] ZnO,[49] and very recently nanographene oxide–TiO_2 PCs.[42] Specifically, tuning the inverse opals PBGs and the associated slow-photon spectral regimes (in water) to the dye electronic absorption, results in the intensification of the self-sensitized degradation mechanism for adsorbed dye molecules at the interface of the high (TiO_2) and low (H_2O) refractive index PC constituents. In the present case, the broad MB absorption band at 664 nm (inset of Fig. S8b, ESI†) approached closely the low energy "red" edge of the 594 nm stop band for PC406 in water (Table 1), where slow-photon propagation and multiple scattering are expected at the anatase skeleton leading to the acceleration of MB

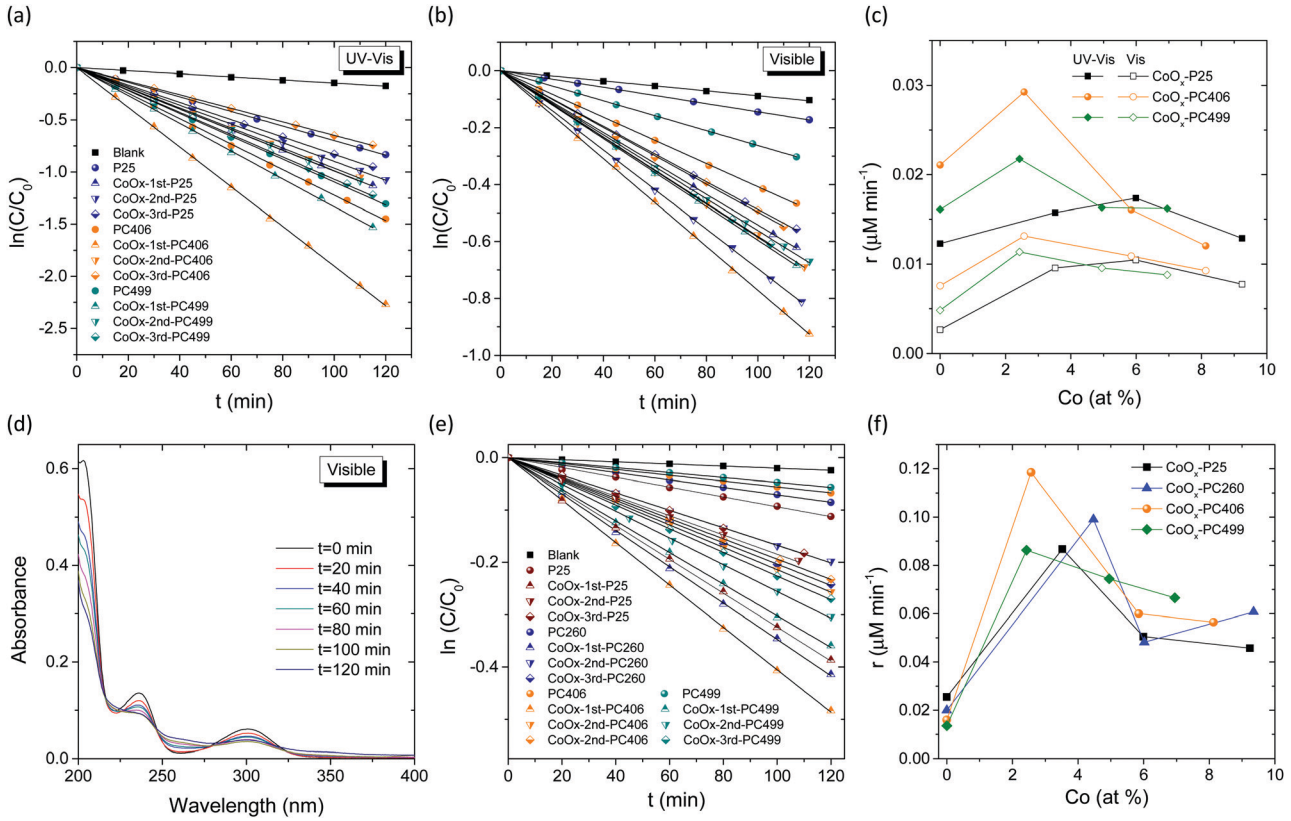

Fig. 6 MB photodegradation kinetics for the pristine and CoO_x-modified PC and P25 films under (a) UV-Vis and (b) visible light and (c) the corresponding reaction rates $r_{UV\text{-}Vis}$ and r_{Vis} as a function of the Co at $\%_x$ loading. (d) SA absorbance spectra evolution for CoO_x-1st-PC406, (e) SA photodegradation kinetics and (f) the reaction rates r_{Vis} as a function of the Co at $\%_x$ loading for all films under visible light.

photodegradation kinetics. Marked variations of the reaction rates were further observed for the CoO_x-modified PC and P25 films, though at different CoO_x loadings (Fig. 6c). The CoO_x-P25 films presented significant increase of $r_{UV\text{-}Vis}$ and r_{Vis} rates reaching a maximum for the 2nd cycle, at ~6 Co at%, confirming the beneficial role of CoO_x–TiO_2 surface complexation in the photocatalytic activity.[22] Even higher increase of $r_{UV\text{-}Vis}$ and r_{Vis} was observed for the 1st cycle CoO_x-PCs, followed by a decline to levels comparable or even lower than those of the pristine ones. This was most pronounced for CoO_x-1st-PC406, which surpassed both CoO_x-1st-PC499 at ~2.5 Co at% and the best CoO_x-2nd-P25, indicating an additional contribution induced by the optimal overlap of slow-photons with the CoO_x electronic absorption.

To discriminate the latter effect, the PC's photocatalytic activity was evaluated on SA degradation under visible light. SA is a colourless water pollutant that absorbs in the UV spectral range (Fig. 6d), far from the inverse opal PBGs, excluding the contribution of slow-photon amplification by molecular dye electronic absorption. In addition, the photocatalytic experiments were conducted at pH = 3 that facilitates SA chemisorption on the TiO_2 surface and direct SA oxidation by valence band holes,[50,51] providing a first assessment of the oxidation ability of photogenerated holes in CoO_x–TiO_2 films under visible light. In all cases, SA photodegradation (Fig. S9a, ESI†), after dark adsorption, followed pseudo-first order kinetics from which the apparent k_{Vis} (Fig. S9b, ESI†) and the reaction rates r_{Vis} (Fig. 6f), were determined as a function of CoO_x loading. Likewise MB degradation, a prominent maximum of r_{Vis} occurred for CoO_x-1st-PC406 at ~2.5 Co at% followed by CoO_x-1st-PC260 at higher CoO_x loading of ~4.5 Co at% and then CoO_x-1st-PC499 and CoO_x-1st-P25 at ~2.5 and ~3.5 Co at%, respectively. It is worth noting that P25 reference films outperformed bare PCs due to the higher catalyst mass as well as the narrower band gap (~3.0 eV) rutile nanocrystals and the VLA-induced interfacial charge transfer to the anatase ones.[52] The observed behaviour can be related to the slow-photon enhancement since both high- and low-energy edges of the PC406 stop band at ~600 nm in water (Table 1) overlap with the broad absorption bands of CoO_x–TiO_2 (Fig. 4). This could lead to slow-light propagation in both the inverse opal skeleton and filled macropores for the PC406 1st films by "red" and "blue" slow photons,[53] respectively, corroborating the photonic amplification of VLA photocatalytic activity by means of the CoO_x surface modification. On the other hand, the corresponding PC499 1st stop band at ~730 nm (Table 1) approached closely the broad Co_3O_4 electronic transition, leading to a modest enhancement and possibly Bragg losses. It is worth noting that PC260 1st presented substantial VLA photocatalytic performance despite the drastic decrease of surface area (Table 2)

with respect to the pristine film. A sizable contribution of "red" slow photons for the 394 nm stop band in water (Table 1) can be accordingly inferred due to the partial overlap with the CoO_x electronic absorption at 420 nm and the anatase absorption edge itself, marginally comprised in the illumination spectral window (400–800 nm). To explore slow-photon enhancement, comparative SA photodegradation experiments were carried for the CoO_x-1st-PC films under narrow band LED irradiation at 405, 450 and 622 nm (S2, ESI†). The corresponding wavelength-dependent reaction rates r_{Vis} are summarized in Fig. S10, ESI.† In the case of CoO_x-1st-PC260, despite a weak maximum of r_{Vis} at 450 nm that may be related to "red" slow photons, its performance was essentially compromised by Bragg losses at 405 nm that falls within its PBG in water (Table 1), while it decreased further at 622 nm due to weak CoO_x absorbance. On the other hand, CoO_x-1st-PC406 presented considerable activity for all wavelengths with an upsurge at 622 nm due to the overlap of its high-energy PBG edge in water with the CoO_x electronic absorption (Fig. 4) due to the preferential formation of single valence CoO and Co_2O_3 oxides. In the case of CoO_x-1st-PC499, r_{Vis} decreased continuously with increasing wavelength following the decrease of CoO_x electronic absorption, since no photonic enhancement could be attained for its ~730 nm PBG in water. It should be noted that no appreciable photocatalytic activity could be detected under visible LED irradiation for the bare PCs confirming the key role of CoO_x on visible light activation. A substantial photonic contribution is accordingly inferred for CoO_x-1st-PC406 that optimally combines slow photon with the electronic absorption and enhanced charge separation (*vide infra*) of low amounts of CoO_x nanoclusters.

Moreover, increase of CoO_x loading for the 2nd and 3rd cycles resulted in the drop of r_{Vis} under broadband visible light, especially for the best performing CoO_x-1st-PC406 and CoO_x-1st-PC260 films (Fig. 6f). This can be associated with detrimental effects arising from the rise of the valence band maximum and the reduction of photogenerated holes' oxidation ability,[19] the unfavourable thermodynamics and aggregation of Co_3O_4 nanocrystals[32,54] with the CC cycles leading to enhanced charge recombination due to its narrow (0.8 eV) direct band gap and/or the suppression of the photonic band structure by absorption losses.[55]

Comparison with available data on PC photocatalytic films[7] shows that CoO_x–TiO_2 PCs present comparable MB degradation rates to those reported for TiO_2 and ZnO PC films based on the VLA dye sensitization mechanism,[48,49] while decomposition of colourless organics such as benzoic acid,[36,48] 4-chlorophenol[49] and Bisphenol A[15] by TiO_2-based PCs was reported only under UV-Vis light. Furthermore, the SA degradation rates compare well to those obtained by intrinsically VLA Bi_2WO_6 inverse opal films[56] and hydrogenated Ag–TiO_2 anodized nanotube arrays,[57] as well as Au–TiO_2 PC films that exploited the unique synergy of plasmonic effects with slow photons for 2,4-dichlorophenol degradation,[58] validating the CoO_x–TiO_2 PC films activity.

The catalysts' stability was evaluated by three consecutive MB photodegradation cycles using the same PC406 1st film under UV-Vis illumination (Fig. S11, ESI†). A rather small decline, less than 6%, of photocatalytic activity was observed. Moreover, SEM measurements after the photocatalytic cycles confirmed that the film retained intact its structural properties, while EDX analyses for the modified films after SA photocatalysis showed minor (<2%) Co losses (Table S1, ESI†) reflecting the strong CoO_x–TiO_2 interfacial coupling on the inverse opal walls. This was corroborated by HR-TEM images for CoO_x-2nd-PC406 after SA photodegradation (Fig. S12, ESI†). The results indicated the persistence of dark nanoscale spots arising primarily from CoO_x aggregates, similar to Fig. 2d, while local EDX elemental analysis confirmed the presence of Co species. In addition, XPS measurements on the CoO_x-3rd-PC499 film after SA photodegradation indicated small losses of Co species (Fig. S13, ESI†). However, no pronounced changes in the Co valence state anticipated by the low crystallinity of CoO_x species[23,24] could be resolved by XPS measurements.

Charge separation

Photoelectrochemical measurements were subsequently applied to investigate the evolution of charge separation with CoO_x loading. Photocurrent transients for the CoO_x-PC406 films deposited on FTO glass substrates under chopped visible light (>420 nm) illumination (Fig. 7a), presented the characteristic "spike and overshoot" features, commonly observed for photoelectrodes with significant surface recombination.[59,60] Upon switching light on, the photocurrent increased almost instantaneously to a sharp peak corresponding to the current density of photogenerated holes (j_h) that reach the semiconductor–electrolyte interface. Subsequently, the photocurrent decayed exponentially to a steady-state value (j_{ss}) due to electron flux and the associated surface recombination current. The negative photocurrent overshoot that followed when switching the light off has been related to the back flow of electrons that recombine with remaining holes at surface states.[55] The CoO_x-1st-PC406 film presented a marked increase of both the instantaneous j_h and steady-state j_{ss} photocurrent densities with respect to the unmodified one, verifying the enhanced visible light harvesting and charge separation induced by slow-photon propagation in combination with low CoO_x loading amounts. On the other hand, j_h and j_{ss} as well as their ratio j_{ss}/j_h, which is a measure of the charge transfer efficiency from the photoelectrode to the electrolyte,[60] decreased successively for the 2nd and 3rd cycle CoO_x-PC406 films despite their increased visible light absorbance due to the higher CoO_x loading and growth of the spinel phase (Fig. 4). This behaviour indicates that surface recombination[61] contributes largely to the decrease of the films' performance after the 2nd and 3rd CC cycles. The latter was further corroborated by EIS measurements performed on the CoO_x-PC406 films under visible light (>420 nm). Fitting the corresponding Nyquist plots (Fig. 7b), indicated that the charge transfer resistance to the electrolyte, reflected in the EIS data curvature, was lowest for CoO_x-1st-PC406 and then increased for the subsequent cycles supporting the optimal charge separation for the 1st CC cycle.

Charge recombination was explored by PL spectroscopy on the CoO_x-PC406 (Fig. 7c) and CoO_x-PC406 (Fig. S14, ESI†) films

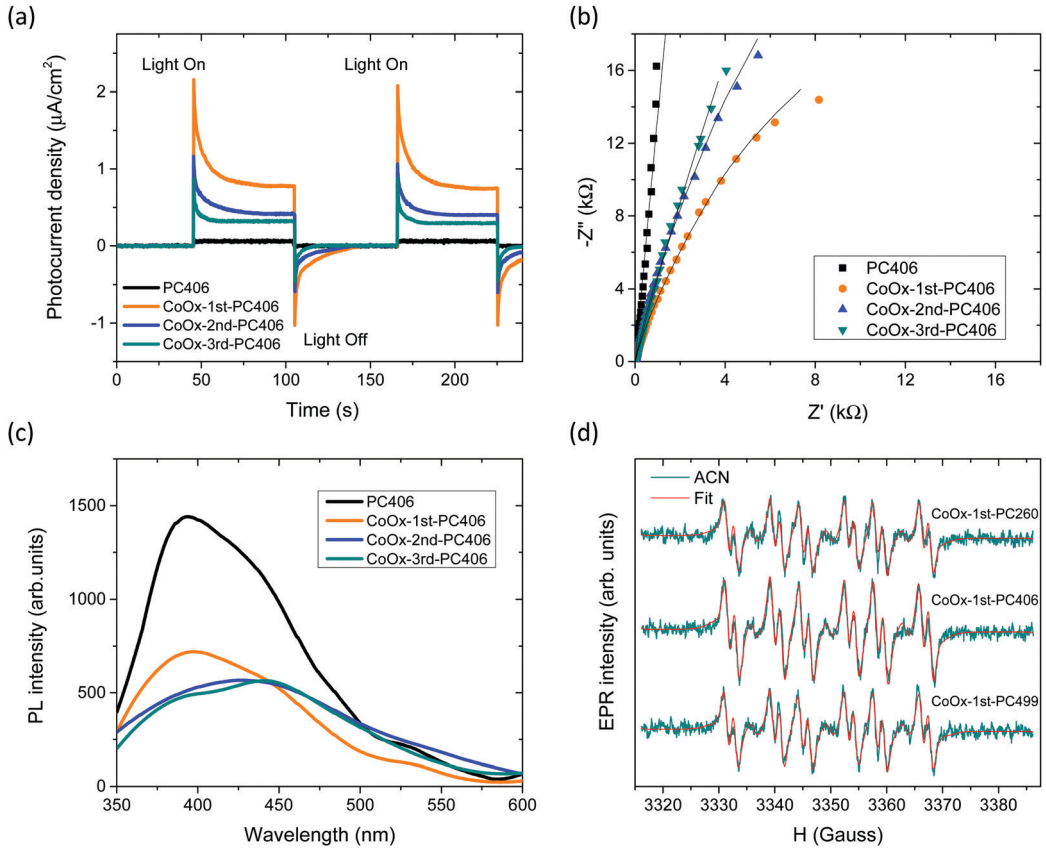

Fig. 7 (a) Transient photocurrent spectra under chopped visible light illumination, (b) EIS Nyquist plots at open circuit, and (c) PL spectra for the CoO_x-PC406 films. (d) DMPO spin trap EPR spectra for the 1st cycle CoO_x-modified PC suspensions in ACN solvent after 4 min visible light illumination. Red lines represent spectral fitting to the experimental EPR spectra by the superposition of DMPO/$O_2^{\bullet-}$, DMPO/$OH^{\bullet}$, DMPO/$OCH_3^{\bullet}$ and degraded DMPO radical adducts (see Fig. S15, ESI† for detailed deconvolution).

under 275 nm excitation. The PL spectra of the pristine PC films presented a broad emission peak at *ca.* 392 nm, which can be attributed to the band-to-band anatase indirect transitions at energies below its absorption edge at 375 nm, accompanied by progressively weaker shoulders at *ca.* 445, 490 and 530–560 nm, related to emission from shallow defect states, such as oxygen vacancies.[62,63] Surface modification of the PC films resulted in the marked drop of the near-band gap PL emission and the defect-induced PL peaks after the 1st CC cycle, supporting the interfacial charge transfer of UV photogenerated electrons to surface states introduced by CoO_x nanoclusters.[22] The PL intensity continued decreasing with the CC cycles, though at a smaller extent for PC406 after the 2nd cycle (Fig. 7c), compared to PC499 (Fig. S14, ESI†).

This behaviour correlates with the formation of Co_3O_4 nanoclusters that appeared in PC406 and PC499 after the 2nd and 3rd cycle, respectively. The persistent PL emission corroborates that excessive CoO_x loading and particularly Co_3O_4 growth may limit further improvement of charge separation by radiative recombination through shallow vacant CoO_x surface states or even from the Co_3O_4 conduction band, which is expected to lie below that of anatase due to the NIR (0.8 eV) direct band gap of the spinel phase.

VLA charge separation on the CoO_x modified photonic films was further assessed by spin trap EPR experiments that allowed the identification of reactive oxygen species (ROS) and particularly hydroxyl ($OH^{\bullet}$) and superoxide ($O_2^{\bullet-}$) radicals using the DMPO spin trap under visible light illumination (Fig. 7d). ROS generation was initially investigated using 1 mg ml^{-1} PC dispersions in the aprotic ACN solvent, in order to increase the $O_2^{\bullet-}$ life time and avoid the conversion of DMPO/$O_2^{\bullet-}$ adduct to DMPO/$OH^{\bullet}$ in aqueous solutions. The formation of both DMPO–superoxide (12–15%) and –hydroxyl (3–4%) radicals could be identified for all 1st cycle CoO_x-PCs under visible light after deconvolution of the composite EPR spectra including the conspicuous DMPO/$OCH_3^{\bullet}$ adduct (76%) and degraded DMPO radical (9%) (Fig. S15a, ESI†). Superoxide radicals may react with ACN and yield the $CH_3COO^{\bullet}$ radical[64] leading to the formation of the DMPO/$OCH_3^{\bullet}$ adduct,[65] which is common in photocatalytic reactions that take place in organic solvents.[66] Although no significant variations could be traced in the relative content of the DMPO radical adducts due to the fast sedimentation of the PC aggregate samples during *ex situ* illumination, the EPR spectra confirmed the VLA generation of $O_2^{\bullet-}$ radicals for the CoO_x modified PCs. On the other hand, the corresponding EPR spectra of aqueous DMPO/PC dispersions presented solely the DMPO/$OH^{\bullet}$ adduct spectrum (Fig. S15b, ESI†), which, however, can be largely due to the very short life time (80 s at pH = 6 and is lowered to 35 s at pH = 8) of DMPO/$O_2^{\bullet-}$ that readily transforms

to DMPO/$OH^{\bullet}$.[67] In order to resolve this matter, experiments were conducted in the presence of 10% of dimethylsulfoxide (DMSO), which is a hydroxyl radical scavenger but does not interfere with the spin trapping of the superoxide radical by DMPO. The results showed a greatly diminished DMPO/$OH^{\bullet}$ adduct formation (Fig. S15b, ESI†) indicating that the observed OH-radical (in the absence of DMSO) is very likely due to water oxidation by the catalyst and to a lesser extent to the conversion of the superoxide adduct to the hydroxyl one. The generation of $OH^{\bullet}$ radicals under visible light was accordingly supported for the modified PCs, validating their potential for photocatalytic applications under visible light.

According to the photocurrent transients, PL and spin trap EPR measurements, it can be inferred that low amounts of highly dispersed CoO_x nanoclusters promote interfacial electron transfer from CoO_x to the anatase nanoparticles under visible light. It should be also noted that the intrinsic catalytic reactivity of CoO_x nanoclusters for water oxidation could also contribute to the enhanced activity.[68] The photo-induced charge transfer is operative under the whole visible spectral range for all the CoO_x–TiO_2 PCs at low CoO_x loading amounts, irrespective of their diameter and PBGs. Combination of these non-selective, advantageous electronic features for CoO_x–TiO_2 inverse opals with the PBG-specific slow photon amplification observed for CoO_x-1st-PC406, underlies the PBG-selective improvement of the VLA photocatalytic performance.

Conclusions

Surface modification of co-assembled TiO_2 photonic crystals was performed by successive chemisorption–calcination cycles of Co acetylacetonate dihydrate with minimal effects on the inverse opal periodicity and photonic properties, which were controlled by the size of the templating colloidal spheres. The formation of nanoscale CoO_x oxides was identified on the nanocrystalline anatase skeleton of the PC films at loading amounts and phase composition that depended on the macropore size and wall mesoporosity. The CoO_x–TiO_2 photonic films presented extended optical absorption in the visible range (400–700 nm), especially at high loading amounts due to the intense charge transfer transitions of the Co_3O_4 spinel phase, which competed with the PC stop band reflectance. Slow photon amplification effects were identified on the photocatalytic degradation of MB and SA probe molecules, when the stop band edges of the surface modified PCs overlapped with the broad CoO_x absorption bands for the 1st CC cycle. The distinct acceleration of photodegradation kinetics, which outperformed similarly modified mesoporous P25 films, was accompanied by analogous photocurrent increase and the identification of hydroxyl ($OH^{\bullet}$) and superoxide ($O_2^{\bullet-}$) radicals under visible light along with reduced charge carrier recombination. The observed improvement was related to the optimal slow-photon-assisted visible light harvesting due to low amounts of CoO_x nanoclusters that also promote charge separation by means of strong interfacial coupling on the titania PC walls. On the other hand, increase of CoO_x loading resulted in the drop of photocatalytic performance pointing to unfavorable thermodynamics and detrimental Co_3O_4 aggregation effects that reinforce charge recombination along with the suppression of photonic amplification by absorption losses that hinder slow light utilization. The obtained results indicate that judicious combination of the photonic crystal properties with compositional tuning of the catalysts' electronic properties by metal oxide heterostructuring is crucial for the development of efficient VLA photonic catalysts featuring enhanced visible light trapping and charge separation.

Conflicts of interest

There are no conflicts to declare.

Acknowledgements

The research work was supported by the Hellenic Foundation for Research and Innovation (H. F. R. I.) under the ''First Call for H. F. R. I. Research Projects to support Faculty members and Researchers and the procurement of high-cost research equipment grant'' (Project Number: 543). A. Toumazatou acknowledges the Onassis Foundation scholarship for doctoral studies and P. Falaras acknowledges support from Prince Sultan Bin Abdulaziz International Prize for Water-Alternative Water Resources Prize 2014.

Notes and references

1 *Photocatalysis: Fundamentals and Perspectives*, ed. J. Schneider, D. Bahnemann, J. Ye, G. Li Puma and D. D. Dionysiou, RSC Energy and Environment Series No. 14, The Royal Society of Chemistry, 2016.
2 A. Fujishima, X. Zhan and D. A. Tryk, *Surf. Sci. Rep.*, 2008, **63**, 515–582.
3 S. Banerjee, S. C. Pillai, P. Falaras, K. E. O'Shea, J. A. Byrne and D. D. Dionysiou, *J. Phys. Chem. Lett.*, 2014, **5**, 2543–2554.
4 G. von Freymann, V. Kitaev, B. V. Lotschz and G. A. Ozin, *Chem. Soc. Rev.*, 2013, **42**, 2528–2554.
5 J. I. Chen, G. von Freymann, S. Y. Choi, V. Kitaev and G. A. Ozin, *Adv. Mater.*, 2006, **18**, 1915–1919.
6 K. R. Phillips, G. T. England, S. Sunny, E. Shirman, T. Shirman, N. Vogel and J. Aizenberg, *Chem. Soc. Rev.*, 2016, **45**, 281–322.
7 V. Likodimos, *Appl. Catal., B*, 2018, **230**, 269–303.
8 J. Yu, J. Lei, L. Wang, J. Zhang and Y. Liu, *J. Alloys Compd.*, 2018, **769**, 740–757.
9 L. Liu, S. Y. Lim, C. S. Law, B. Jin, A. D. Abell, G. Ni and A. Santos, *J. Mater. Chem. A*, 2019, **7**, 22514–22529.
10 A. Stein, B. E. Wilson and S. G. Rudisill, *Chem. Soc. Rev.*, 2013, **42**, 2763–2803.
11 C. W. Cheng, S. K. Karuturi, L. J. Liu, J. P. Liu, H. X. Li, L. T. Su, A. I. Y. Tok and H. J. Fan, *Small*, 2012, **8**, 37–42.
12 S. Guo, D. Li, Y. Zhang, Y. Zhang and X. Zhou, *Electrochim. Acta*, 2014, **121**, 352–360.

13 R. Mitchell, R. Brydson and R. E. Douthwaite, *Phys. Chem. Chem. Phys.*, 2015, **17**, 493–499.
14 C. Li, X. Zhu, H. Zhang, Z. Zhu, B. Liu and C. Cheng, *Adv. Mater. Interfaces*, 2015, **2**, 1500428.
15 Z. Geng, Y. Zhang, X. Yuan, M. Huo, Y. Zhao, Y. Lu and Y. Qiu, *J. Alloys Compd.*, 2015, **644**, 734–741.
16 K. Zhang, Y. Liu, J. Deng, S. Xie, H. Lin, X. Zhao, J. Yang, Z. Han and H. Dai, *Appl. Catal., B*, 2017, **202**, 569–579.
17 M. Zalfani, Z.-Y. Hu, W.-B. Yu, M. Mahdouani, R. Bourguiga, M. Wu, Y. Li, G. Van Tendeloo, Y. Djaoued and B.-L. Su, *Appl. Catal., B*, 2017, **205**, 121–132.
18 H. Tada, Q. Jin, A. Iwaszuk and M. Nolan, *J. Phys. Chem. C*, 2014, **118**, 12077–12086.
19 H. Tada, Q. Jin, H. Nishijima, H. Yamamoto, M. Fujishima, S.-I. Okuoka, T. Hattori, Y. Sumida and H. Kobayashi, *Angew. Chem., Int. Ed.*, 2011, **50**, 3501–3505.
20 C. Y. Wang, D. W. Bahnemann and J. K. Dohrmann, *Chem. Commun.*, 2000, 1539–1540.
21 M. Nolan, A. Iwaszuk and H. Tada, *Aust. J. Chem.*, 2012, **65**, 624–632.
22 Q. Jin, H. Yamamoto, K. Yamamoto, M. Fujishima and H. Tada, *Phys. Chem. Chem. Phys.*, 2013, **15**, 20313–20319.
23 A. Bergmann, E. Martinez-Moreno, D. Teschner, P. Chernev, M. Gliech, J. F. de Araújo, T. Reier, H. Dau and P. Strasser, *Nat. Commun.*, 2015, **6**, 8625.
24 J. Yang, J. K. Cooper, F. M. Toma, K. A. Walczak, M. Favaro, J. W. Beeman, L. H. Hess, C. Wang, C. Zhu, S. Gul, J. Yano, C. Kisielowski, A. Schwartzberg and I. D. Sharp, *Nat. Mater.*, 2017, **16**, 335.
25 J. R. Ran, J. Zhang, J. G. Yu, M. Jaroniec and S. Z. Qiao, *Chem. Soc. Rev.*, 2015, **46**, 7787–7812.
26 G. Dong, H. Hu, X. Huang, Y. Zhang and Y. Bi, *J. Mater. Chem. A*, 2018, **6**, 21003–21009.
27 L. Qiao, H. Y. Xiao, H. M. Meyer, J. N. Sun, C. M. Rouleau, A. A. Puretzky, D. B. Geohegan, I. N. Ivanov, M. Yoon, W. J. Weber and M. D. Biegalski, *J. Mater. Chem. C*, 2013, **1**, 4628–4633.
28 V. Singh, M. Kosa, K. Majhi and D. T. Major, *J. Chem. Theory Comput.*, 2015, **11**, 64–72.
29 V. Singh and D. T. Major, *Inorg. Chem.*, 2016, **55**, 3307–3315.
30 S. B. Cho, E. S. Sim and Y. C. Chung, *J. Eur. Ceram. Soc.*, 2018, **38**, 629–635.
31 J. Wang and F. E. Osterloh, *J. Mater. Chem. A*, 2014, **2**, 9405–9411.
32 K. Maeda, K. Ishimaki, M. Okazaki, T. Kanazawa, D. Lu, S. Nozawa, H. Kato and M. Kakihana, *ACS Appl. Mater. Interfaces*, 2017, **9**, 6114–6122.
33 D. Lang, F. Cheng and Q. Xiang, *Catal. Sci. Technol.*, 2016, **6**, 6207–6216.
34 S. Bala, I. Mondal, A. Goswami, U. Pal and R. Mondal, *J. Mater. Chem. A*, 2015, **3**, 20288–20296.
35 B. Hatton, L. Mishchenko, S. Davis, K. H. Sandhage and J. Aizenberg, *Proc. Natl. Acad. Sci. U. S. A.*, 2010, **107**, 10354–10359.
36 Z. Cai, Z. Xiong, X. Lu and J. Teng, *J. Mater. Chem. A*, 2014, **2**, 545–553.
37 S. Ito, P. Chen, P. Comte, M. K. Nazeeruddin, P. Liska, P. Pechy and M. Grätzel, *Prog. Photovoltaics*, 2007, **15**, 603–612.
38 K. R. Phillips, T. Shirman, E. Shirman, A. V. Shneidman, T. M. Kay and J. Aizenberg, *Adv. Mater.*, 2018, **30**, 1706329.
39 J. Du, X. Lai, N. Yang, J. Zhai, D. Kisailus, F. Su, D. Wang and L. Jiang, *ACS Nano*, 2011, **5**, 590–596.
40 S. Balaji, Y. Djaoued and J. Robichaud, *J. Raman Spectrosc.*, 2006, **37**, 1416–1422.
41 V. Likodimos, T. Stergiopoulos, P. Falaras, J. Kunze and P. Schmuki, *J. Phys. Chem. C*, 2008, **112**, 12687–12696.
42 A. Diamantopoulou, E. Sakellis, G. E. Romanos, S. Gardelis, N. Ioannidis, N. Boukos, P. Falaras and V. Likodimos, *Appl. Catal., B*, 2019, **240**, 277–290.
43 Y. Li, W. Qiu, F. Qin, H. Fang, V. G. Hadjiev, D. Litvinov and J. Bao, *J. Phys. Chem. C*, 2016, **120**, 4511–4516.
44 Z. Wang, H. Dong, X. Huang, Y. Mo and L. Chen, *Electrochem. Solid-State Lett.*, 2004, **7**, A353–A357.
45 B. Rivas-Murias and V. Salgueiriño, *J. Raman Spectrosc.*, 2017, **48**, 837–841.
46 B. J. Tan, K. J. Klabunde and P. M. A. Sherwood, *J. Am. Chem. Soc.*, 1991, **113**, 855–861.
47 A. Houas, H. Lachheb, M. Ksibi, E. Elaloui, C. Guillard and J. M. Hermann, *Appl. Catal., B*, 2001, **31**, 145–157.
48 X. Zheng, S. Meng, J. Chen, J. Wang, J. Xian, Y. Shao, X. Fu and D. Li, *J. Phys. Chem. C*, 2013, **117**, 21263–21273.
49 S. Meng, D. Li, P. Wang, X. Zheng, J. Wang, J. Chen, J. Fang and X. Fu, *RSC Adv.*, 2013, **3**, 17021–17028.
50 S. Tunesi and M. Anderson, *J. Phys. Chem.*, 1991, **95**, 3399–3405.
51 A. Diamantopoulou, E. Sakellis, S. Gardelis, D. Tsoutsou, S. Glenis, N. Boukos, A. Dimoulas and V. Likodimos, *Materials*, 2019, **12**, 2518.
52 V. Likodimos, A. Chrysi, M. Calamiotou, C. Fernández-Rodríguez, J. M. Doña-Rodríguez, D. D. Dionysiou and P. Falaras, *Appl. Catal., B*, 2016, **192**, 242–252.
53 O. Deparis, S. R. Mouchet and B. L. Su, *Phys. Chem. Chem. Phys.*, 2015, **17**, 30525–30532.
54 K. Ishimaki, T. Uchiyama, M. Okazaki, D. Lu, Y. Uchimoto and K. Maeda, *Bull. Chem. Soc. Jpn.*, 2018, **91**, 486–491.
55 G. von Freymann, S. John, M. Schulz-Dobrick, E. Vekris, N. Tetreault, S. Wong, V. Kitaev and G. A. Ozin, *Appl. Phys. Lett.*, 2004, **84**, 224–226.
56 L. W. Zhang, C. Baumanis, L. Robben, T. Kandiel and D. Bahnemann, *Small*, 2011, **7**, 2714–2720.
57 Y. Lu, H. Yu, S. Chen, X. Quan and H. Zhao, *Environ. Sci. Technol.*, 2012, **46**, 1724–1730.
58 M. Plodinec, I. Grcic, M. G. Willinger, A. Hammud, X. Huang, I. Panzic and A. Gajovi, *J. Alloys Compd.*, 2019, **776**, 883–896.
59 C. Y. Cummings, F. Marken, L. M. Peter, A. A. Tahir and K. G. U. Wijayantha, *Chem. Commun.*, 2012, **48**, 2027–2029.
60 D. Klotz, D. A. Grave and A. Rothschild, *Phys. Chem. Chem. Phys.*, 2017, **19**, 20383–20392.
61 H. K. Dunn, J. M. Feckl, A. Müller, D. Fattakhova-Rohlfing, S. G. Morehead, J. Roos, L. M. Peter, C. Scheu and T. Bein, *Phys. Chem. Chem. Phys.*, 2014, **16**, 24610–24620.
62 N. Serpone, D. Lawless and R. Khairutdinov, *J. Phys. Chem.*, 1995, **99**, 16646–16654.

63 T. Toyoda, W. Yindeesuk, T. Okuno, M. Akimoto, K. Kamiyama, S. Hayase and Q. Shen, *RSC Adv.*, 2015, **5**, 49623–49632.
64 M. Cervera and J. Marquet, *Can. J. Chem.*, 1998, **76**, 966–969.
65 V. Brezová, S. Gabčová, D. Dvoranová and A. Staško, *J. Photochem. Photobiol., B*, 2005, **79**, 121–134.
66 D. Dvoranova, Z. Barbierikova and V. Brezova, *Molecules*, 2014, **19**, 17279–17304.
67 E. Finkelstein, G. M. Rosen and E. J. Rauckman, *Mol. Pharmacol.*, 1982, **21**, 262–265.
68 M. Okazaki, Y. Wang, T. Yokoi and K. Maeda, *J. Phys. Chem. C*, 2019, **123**, 10429–10434.

